# The Effect of Alloy Composition and Welding Conditions on Columnar-Equiaxed Transitions in Ferritic Stainless Steel Gas-Tungsten Arc Welds

J.C. VILLAFUERTE, E. PARDO, and H.W. KERR

The columnar-equiaxed transition (CET) was investigated in full penetration gas-tungsten arc (GTA) welds on ferritic stainless steel plates containing different amounts of minor elements, such as titanium and aluminum, for a range of welding conditions. In general, the fraction of equiaxed grains increased, and the size of the equiaxed grains decreased with increasing titanium contents above 0.18 wt pct. At a given level of titanium, the equiaxed fraction increased, and the size of the equiaxed grains decreased with increased aluminum content. The CET was ascribed to heterogeneous nucleation of ferrite on Ti-rich cuboidal inclusions, since these inclusions were observed at the origin of equiaxed dendrites in the grain refined welds. Titanium-rich cuboidal inclusions, in turn, were found to contain Al-Ca-Mg-rich inclusions at their centers, consistent with observations by previous investigators for other processes. The welding conditions, in particular, the welding speed, were observed to affect the occurrence of the CET. Increasing the welding speed from 3 to 8 mm/s increased the equiaxed fraction noticeably, but a further increase in speed to 14 mm/s had a smaller additional effect. A finite element model (FEM) of heat transfer was used to examine the role of the welding conditions on the local solidification conditions along the weld pool edge. The results are compared with existing models for the CET.

## I. INTRODUCTION

WELD pool solidification can readily start from the parent metal partially molten zone with a minimum degree of undercooling. This leads to the well-known epitaxial growth, rather than requiring any nucleation event, resulting in a coarse columnar grain structure with a preferred orientation. The deleterious influence of this normal weld pool solidification upon certain mechanical properties of the weld deposit has stimulated research into weld pool solidification. In particular, the formation of a central equiaxed zone helps to prevent both centerline hot cracking[1] and a weak centerline in subsequent plastic deformation.

Several mechanisms have been proposed to assist the columnar-equiaxed transition (CET) during weld pool solidification, including dendrite fragmentation,[2,3,4] grain detachment,[5] and heterogeneous nucleation.[5,6,7] In aluminum gas-tungsten arc (GTA) welds, Kerr and coworkers[5,6] and later Kou and Le[7,8] observed that Ti-rich particles act as heterogeneous nucleation sites. Pearce and Kerr[5] have also proposed partially molten zone grain detachment as a second refining mechanism for some alloys. On the other hand, Matsuda *et al.*[2,3,9] proposed dendrite fragmentation as the mechanism to explain the occurrence of equiaxed grains in aluminum and austenitic stainless GTA welds containing titanium.

J.C. VILLAFUERTE, Graduate Student, and H.W. KERR, Professor, are with the Department of Mechanical Engineering, University of Waterloo, Waterloo, ON N2L 3G1, Canada. E. PARDO, formerly Postdoctoral Fellow, Department of Mechanical Engineering, University of Waterloo, is Adjoint Professor of Mechanics, Faculty of Engineering, Institute of Materials Science and Technology (INTEMA), University of Mar del Plata, 7600 Mar del Plata, Argentina.

Manuscript submitted August 16, 1989.

The role of titanium as a nucleant in cast steels, which cool more slowly than GTA welds, has beeen known for some time. Bramfitt[10] reported that titanium nitrides and carbides were effective in promoting equiaxed grains in iron due to heterogeneous nucleation of $\delta$-Fe on these phases. In mild steel submerged arc (SA) welds, Turnbull *et al.*[11] used a hollow electrode containing Fe-Ti and TiC mixtures to refine the grain size. Garland[12] reported grain refinement in mild steel SA welds by inoculating with Fe-Ti mixtures. The effect was ascribed to heterogeneous nucleation on TiC. Willingham and Bailey[13] used additions of Fe-Ti, $TiB_2$, and mixtures of $TiB_2$ + $CaF_2$ in grain-refining SA welds. Ostrowski and Langer[14] reported grain refinement in cast ferritic Fe-17 pct Cr stainless steel due to heterogeneous nucleation of $\delta$-ferrite on Ti-rich inclusions. For this to occur, the Ti-rich inclusions first must be nucleated. Ostrowski and Langer proposed a complex heterogeneous nucleation process of TiN or Ti(C, N) on high-temperature oxides, including $Al_2O_3$, $SiO_2$, $Ti_xO_y$, $Y_2O_3$, or $ZrO_2$, with the nucleation of sulfide layers third. The heterogeneous nucleation of $\delta$-ferrite on the sulfide-rich surfaces of Ti-rich inclusions was proposed to be responsible for the refinement effect of the metal phase.

Heintze and McPherson[15] reported that Ti additions in high-strength low-alloy (HSLA) and stainless steel SA welds were effective in refining the grain size if the primary phase was ferrite but not if the primary phase was austenite. The refinement effect was attributed to the nucleation of ferrite in TiN particles, and the effectiveness of TiN was ascribed to the low disregistry between TiN and ferrite. They proposed that TiN inclusions were nucleated on $Al_2O_3$ following a formation sequence similar to that suggested by Ostrowski and Langer[14] in ingots. However, in this case, Heintze and McPherson did not

find evidence of sulfide compounds on the surfaces of Ti-rich particles.

Hence, although there is some evidence that titanium additions promote an equiaxed zone in some steels, the effects and the mechanism(s) are unclear, particularly in GTA welds. The present work was undertaken to clarify the effects of titanium and aluminum additions, as well as the welding conditions, for ferritic stainless steel GTA welds. In order to interpret the effects of welding conditions, a thermal model was developed using the finite element method.

## II. EXPERIMENTAL PROCEDURE

Full-penetration bead-on-plate GTA welds were produced in ferritic stainless steel sheet. The voltage was measured between the electrode holder and the welding table, and the current was measured using a shunt connected in series with the electrode cable. The current return at the rear of the weld pool was ensured by using a copper strip contact, with the remainder of the sheet electrically isolated with asbestos. The welding conditions are shown in Table I.

Welding samples were cut from 2 mm-thick sheets of type 409 ferritic stainless steel and one experimental steel, containing different amounts of Ti, Al, C, and N. The chemical compositions are shown in Table II.

To examine the macrostructure, the surfaces to be observed were ground with 600 grade emery paper prior to etching. A reagent made of 340 g Fe $Cl_3 \cdot 6H_2O$, 125 ml HCl, 40 ml $HNO_3$, and 250 ml $H_2O$ was used to reveal the weld macrostructures by swabbing the surface for about 30 seconds.

The fraction of equiaxed grains at the top surface was obtained from at least ten measurements, using the ratio of the widths of the equiaxed zone and the weld pool. The existence of a true equiaxed zone through the thickness was verified using cross sections, since at low titanium levels it was observed that surface nucleation can occur prior to equiaxed grain formation through the thickness of the sheet. The equiaxed fractions at the midplane were measured using at least five sections for each weld. Diameters of equiaxed grains were also measured at the weld top surfaces, using an average of at least 20 measurements.

More detailed observations of the microstructure were made using both light optical microscopy (LOM) and scanning electron microscopy (SEM). In ferritic stainless steels, most recommended reagents revealed only the grain boundaries and not the solidification substructure. A solution made from 40 g $FeCl_3 \cdot 6H_2O$, 3 g $CuCl_2$, 40 ml HCl, and 500 ml $H_2O$[16] provided the best results. Both the grain boundaries and the solidification substructure were revealed by swabbing for 20 to 30 seconds. Energy dispersive X-ray (EDX) microanalyses were performed on different types of inclusions in unetched specimens, usually after ion-beam etching. The inclusion spectra were processed by subtracting the matrix spectra (FeK-$\alpha$ and CrK-$\alpha$ peaks) from the inclusion spectra to eliminate X-rays excited within the matrix. Standardless atomic number, absorption, and fluorescence corrections were made on the remaining peaks. The EDX analyzer was not capable of detecting nitrogen or oxygen percentages. The average results for similar measured compositions give a semiquantitative summary of typical inclusion compositions in a given steel, which can be multiphased.[15]

**Table I. Welding Conditions**

| | |
|---|---|
| Process: | direct current "straight polarity" (electrode negative) (DCSP) bead-on-plate, full penetration GTA weld |
| Position: | flat |
| Welding speed: | 3 mm/s, 8 mm/s, 14 mm/s |
| Electrode: | W-2 pct Th, 60 cone included angle |
| Diameter: | 2.38 mm (3/32 in.) for 3 and 8 mm/s<br>3.175 mm (1/8 in.) for 14 mm/s |
| Arc length: | 2 mm |
| Electrode stickout: | 3 mm |
| Torch position: | vertical |
| Upper shielding: | Ar 99.9 pct, flow rate 0.27 $dm^3/s$ (35 CFH) |
| Underneath shielding: | Ar 99.9 pct, flow rate 0.31 $dm^3/s$ (40 CFH) |

## III. FINITE ELEMENT MODEL

The CET was found to depend on both the composition and the welding conditions. The influence of the welding conditions is related to changes in the temperature gradient, $G$, and the local solidification velocity, $R$, at the solid-liquid interface along the weld pool edge.[1,6,8] Analytical expressions for the local values of $G$ and $R$ are available[17] but ignore the effects of the latent heat of fusion, the distribution of the heat input, the temperature dependence of the thermal conductivity, and other factors. Hence, previous discussions of the CET[6,8] have utilized relatively crude estimates of the values of $G$ and $R$. In order to estimate values of $G$ and $R$ more accurately, a steady-state heat transfer model of the process was formulated in a coordinate framework moving with the welding arc.

A finite element code was used, based on a code described elsewhere[18] but modified for the present GTA

**Table II. Chemical Analysis of Steels (Weight Percent)**

| Steel | Cr | Ni | C | Ti | Al | Mn | Si | S | N |
|---|---|---|---|---|---|---|---|---|---|
| 9795 | 31.80 | <1.0 | 0.025 | 0.01 | 0.108 | 0.79 | 0.65 | <0.001 | 0.059 |
| 4093 | 11.06 | 0.34 | 0.004 | 0.18 | 0.012 | 0.50 | 0.50 | 0.007 | 0.006 |
| 4092 | 10.97 | 0.19 | 0.009 | 0.29 | 0.010 | 0.42 | 0.48 | 0.002 | 0.007 |
| 4091 | 11.25 | 0.18 | 0.008 | 0.32 | 0.035 | 0.48 | 0.43 | 0.002 | 0.005 |
| 4094 | 11.39 | 0.22 | 0.012 | 0.29 | 0.040 | 0.30 | 0.42 | 0.002 | 0.016 |
| 4095 | 11.44 | 0.27 | 0.012 | 0.36 | 0.044 | 0.31 | 0.43 | 0.002 | 0.016 |

welding process. This code includes the latent heat of fusion, which was modeled as a parabolic contribution to the specific heat, instead of as a sudden increase in specific heat. The position of the solid-liquid interface was assumed to be defined by the "pinch-off" temperature.[19]

The liquid thermal conductivity was artifically enhanced to account for fluid motion. The welding arc was modeled as an imposed heat flux with a Gaussian distribution.

## IV. RESULTS

### A. *Equiaxed Grain Fractions and Sizes*

The observed fraction of equiaxed grains was a function of welding speed, titanium content, and aluminum content. At the lowest welding speed, 3 mm/s, very few equiaxed grains were observed until the titanium content was greater than 0.18 wt pct, as illustrated in Figure 1. The measured fractions of equiaxed grains at the top surfaces are given for most steels in Figure 2. In general, the equiaxed fraction at the surface increased with titanium content above 0.18 wt pct.

Within the equiaxed zone, the grain size was dependent on the titanium content; higher titanium levels tended to produce finer grain sizes (Figure 3). The effect of titanium on the grain size was also evident in the weld craters when the arc was extinguished, where it was observed that more titanium reduced the grain size and increased the extent of the central equiaxed zone. For the lower titanium levels, the combination of small equiaxed fractions and large equiaxed grains resulted in an equiaxed zone only 1 to 3 grains wide.

At a given titanium level, the equiaxed fraction also depended on the content of other minor additions, notably aluminum. For a titanium content of 0.29 wt pct, an increase in aluminum content from 0.010 to 0.040 wt pct resulted in a significant increase in the equiaxed fraction, as shown in Figure 4. The equiaxed grain size also decreased with increased aluminum, as illustrated in Figure 5. At the higher welding speeds (8 and 14 mm/s), the equiaxed fraction observed at the surface of a given steel was generally greater than that observed at the lowest speed. This effect of welding speed is illustrated in Figure 6 for the steel containing 0.32 pct titanium. The results for all steels are summarized in Figures 2 and 4.

However, the grain structures observed at the surface could be misleading, especially in steels with low titanium levels. Cross sections of these steels showed that even at the highest welding speed, the grain refinement observed at the surface did not occur through the thickness of the weld. Columnar grains from the fusion boundary persisted in the midplane region of these low titanium steels, as illustrated in Figure 7(a) and summarized in Table III. However, in the steels containing at least 0.29 pct Ti and 0.040 pct Al, the equiaxed grain structure at the surface was also observed through the thickness of the sheet, as illustrated in Figure 7(b) and summarized in Table III.

The equiaxed grain size generally decreased with increased welding speed. The effects at a constant titanium content (0.29 wt pct) are shown in Figure 5. The effects of welding speed for different titanium levels are given in Figure 4, which shows that welding speed had less effect at high titanium levels than at low titanium contents.

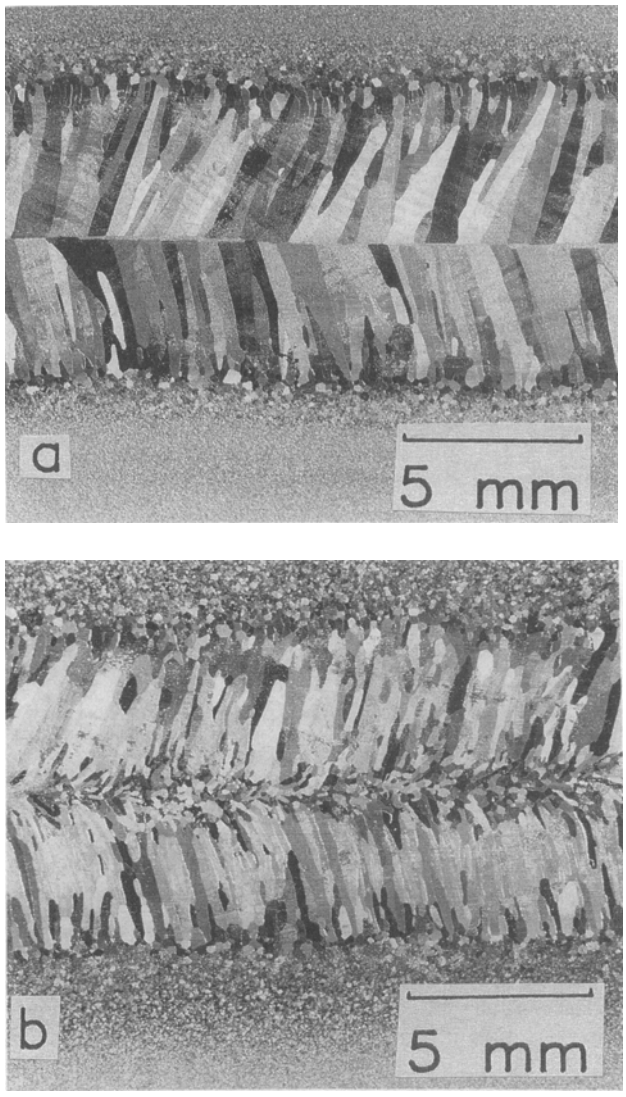


Fig. 1—Surface grain structures in welds made at 3 mm/s in (*a*) steel 4093 (0.18 wt pct Ti, 0.012 wt pct Al) and (*b*) steel 4095 (0.36 wt pct Ti, 0.044 wt pct Al).

### B. *Inclusions and Grain Refinement*

The results above show that the compositions of the ferritic stainless steels, particularly the titanium and aluminum contents, strongly influence the equiaxed fractions. Equiaxed grains were examined in several welds, using various chemical etches and ion beam etching. In order to observe the dendritic solidification structure, a strong chemical etchant must be employed. In many cases, this etching appeared to remove central particles, leaving only a pit. However, by successive etching and careful polishing, particles were observed at the centers of some dendrites, as illustrated in Figure 8. Similar observations were made using ion-beam etching to reveal the solidification structure and particles, followed by Nomarski contrast techniques in the optical microscope (Figure 9).

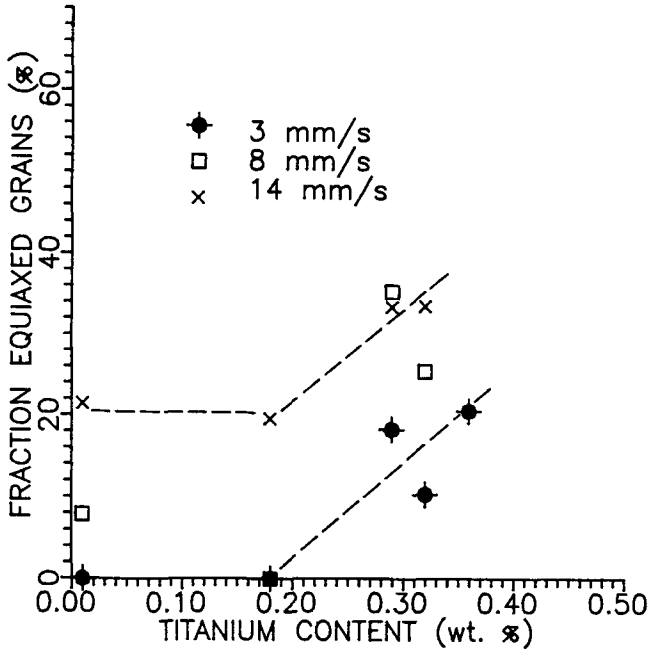


Fig. 2—Average equiaxed grain fractions observed at the surfaces of all steels except 4092 *vs* titanium content.

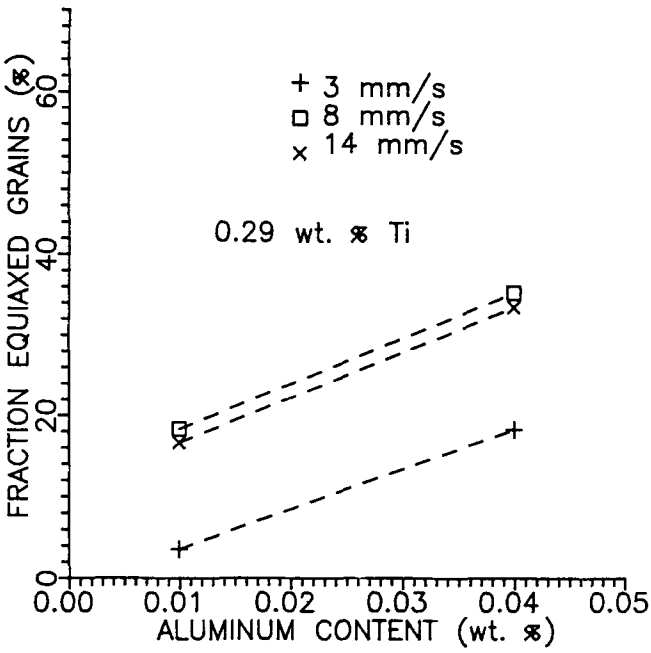


Fig. 4—Average equiaxed grain fraction observed at the surfaces of steels containing 0.29 wt pct Ti *vs* aluminum content.

Scanning electron microscopy generally did not reveal the dendrite solidification structure and could not be used to correlate inclusion locations with solidification.

Many of the observed particles were not at the centers of dendrites. In some cases, several particles were found in the same equiaxed grain. Heintze and McPherson[15] also have reported apparent heterogeneous nucleation on some, but not all, inclusions in stainless steel SA welds.

The particles in various welds were examined at higher magnification in the as-polished condition. Two different kinds of inclusions were observed, which, due to their typical shapes, were classified as either cuboidal or spherical. Cuboidal inclusions appeared yellowish in the optical microscope, whereas spherical inclusions were gray or brown. In most cuboidal inclusions, a central subparticle was observed. A typical example of a cuboidal particle with a central spherical region is shown in Figure 10. Energy dispersive X-ray spectra obtained when the beam was located directly on the central spherical region showed peaks in titanium, as well as various combinations of aluminum, calcium, magnesium, and/or sulfur. When the beam was located on the cuboidal portion of these inclusions, much stronger titanium peaks were observed. The results, summarized in Table IV, show that the cuboidal regions could be as high as 100 pct titanium, whereas the central particles always contained other metallic elements. The X-ray spectra recorded at the central subparticles depended on the levels

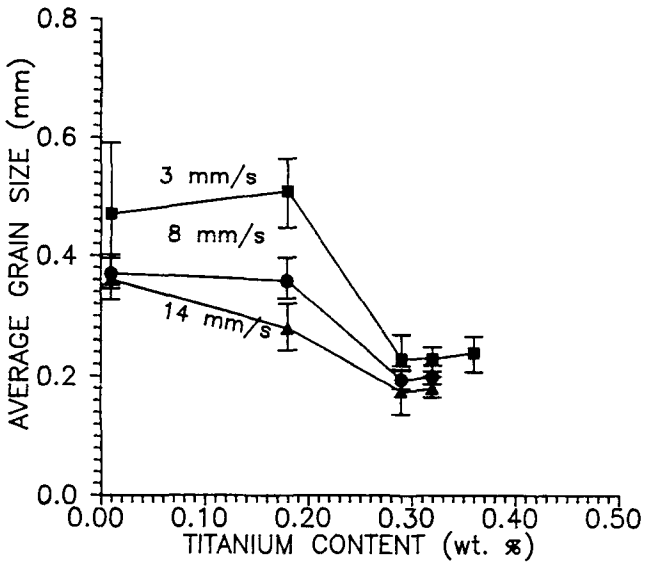


Fig. 3—Surface equiaxed grain size *vs* titanium content (excluding steel 4092).

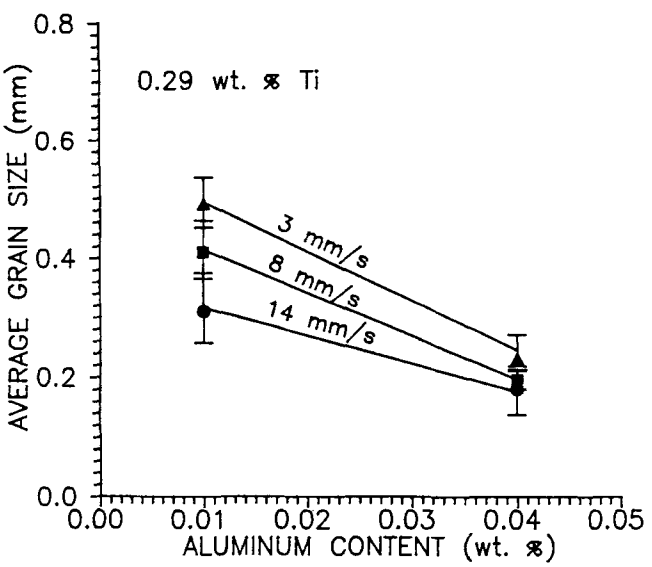


Fig. 5—Surface equiaxed grain size *vs* aluminum content in steels containing 0.29 wt pct titanium.

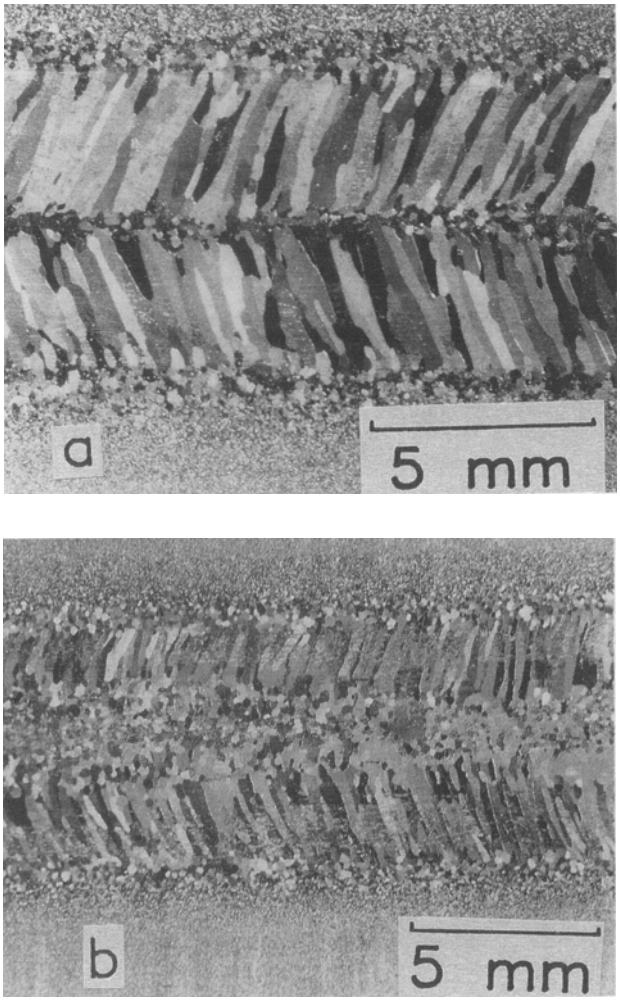


Fig. 6—Grain structures observed at the surfaces of welds containing 0.32 wt pct titanium welded at (*a*) 3 mm/s and (*b*) 14 mm/s.

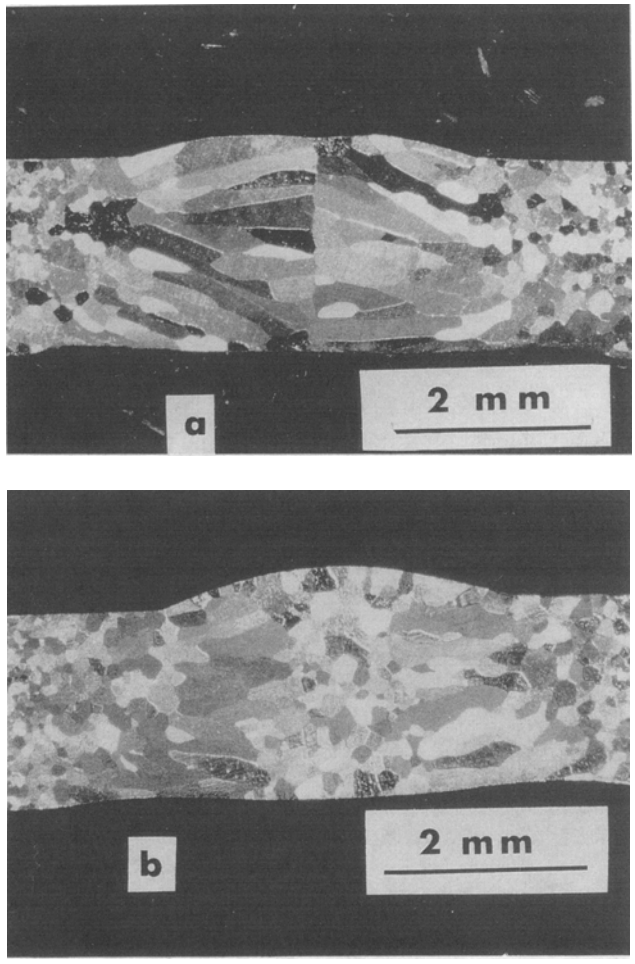


Fig. 7—Cross sections of welds made at 14 mm/s containing (*a*) 0.18 wt pct Ti, 0.012 wt pct Al and (*b*) 0.32 wt pct Ti, 0.035 wt pct Al.

of minor elements of the steel being analyzed. For example, several spectra corresponding to central subparticles in steel 4093 showed sulfur peaks, consistent with the fact that this steel had the highest sulfur content (0.007 wt pct) of the steels analyzed.

Spherical inclusions were observed in those steels (4091, 4092, and 4093) with low average C and N contents. Energy dispersive X-ray spectra obtained from these inclusions, also summarized in Table IV, indicated that their main components were Al, Ca, Mg, and Ti. The occurrence of certain peaks appeared to be related to the content of minor elements. For example, in steel 4091 (with the highest Al and Ti content of this series), Al, Ca, Ti, and, in some cases, Mg, were more evident, whereas for lower average aluminum and titanium contents (steels 4092 and 4093), only calcium and titanium peaks were present.

The numbers of these small particles were difficult to determine quantitatively. In general, many coarse (around 5 microns) and small (around 1 micron) cuboidal particles were observed in the high nitrogen and titanium samples, whereas mostly small particles were in the low nitrogen samples. Many small cuboids were found in the steels with relatively high aluminum and titanium contents, even when the nitrogen content was low.

A closer observation of small spherical inclusions under better resolution conditions (gold coating and small working distance in the scanning electron microscope) revealed an outer rim in most of these inclusions. This is illustrated in Figure 11. Unfortunately, the parameters required for optimal X-ray acquisition in the scanning electron microscope are inconsistent with the parameters to obtain a high resolution image. The titanium peaks collected in spectra from small isolated spherical particles may be due to this Ti-rich outer rim in its early stage of growth.

### C. *Numerical Results*

Best agreement between the finite element model and observed weld dimensions was obtained by increasing the heat source radius, consistent with Reference 20, while the arc efficiency was decreased. The parameters used to estimate thermal conditions in the actual welds are listed in Table V.

The derived thermal gradient, which is a minimum at the weld pool tail, decreases with welding speed, as shown

**Table III. Equiaxed Fractions at Surface and Midplanes (Average and Standard Deviations)**

| | 3 mm/s | | 8 mm/s | | 14 mm/s | |
|---|---|---|---|---|---|---|
| Steel | Top | Mid | Top | Mid | Top | Mid |
| 9795 | 0 | 0 | 7.8* ± 10.8 | 0 | 21.4* ± 5.0 | 0 |
| 4093 | 0 | 0 | 0 | 0 | 19.6* ± 9.0 | 0 |
| 4092 | 3.6* ± 6.2 | 0 | 18.3* ± 9.0 | 0 | 16.6* ± 7.0 | 0 |
| 4094 | 18.3 ± 8.4 | 11.7 ± 5.5 | 35.4 ± 7.0 | 33.6 ± 5.0 | 29.8 ± 6.0 | — |
| 4091 | 10.3* ± 4.2 | 9.3 ± 3.2 | 25.5 ± 7.0 | 23.4 ± 8.8 | 33.5 ± 7.0 | 29.5 ± 5.5 |
| 4095 | 20.6 ± 4.9 | 16.3 ± 4.5 | — | — | — | — |

*1 to 3 grains in width of equiaxed zone.

in Table VI. This trend is consistent with the prediction of Rosenthal's solution, from which the following simplified expression may be derived:[17]

$$G_c = 2\pi k\rho c_p \left(\frac{h}{q}\right)^2 v(T_p - T_0)^3 \qquad [1]$$

where $h$ is plate thickness, $q$ is input power, and $T_0$ is the preheating temperature. There are, however, some fundamental differences that are worth pointing out. The exchange of latent heat of fusion between solid and liquid, which is neglected in the analytical solution, has a strong effect on thermal gradients around the weld pool edge as well as on the weld pool dimensions.

The total change in thermal gradient across the melting range is proportional to the solidification velocity and the latent heat of fusion. Hence, the approximation given by Eq. [1] overestimates the thermal gradient on the solidification front by an amount proportional to the solidification rate. Radiation from the surface further decreases this thermal gradient. Its effect is expected to be higher at the surface, consistent with the observed surface grain refinement in some samples.

The predicted local solidification velocities, $R$, and thermal gradients, $G$, (as defined in Figure 12) are given in Figures 13 and 14 for the three welding speeds as a function of distance from the centerline. The solidification velocity, $R$, is predicted to increase as solidification proceeds from the fusion boundary but reaches a plateau before increasing toward the end of solidification. The temperature gradients, $G$, close to the centerline are predicted to decrease slightly with increased welding speed and are much higher at the fusion boundary (Figure 14).

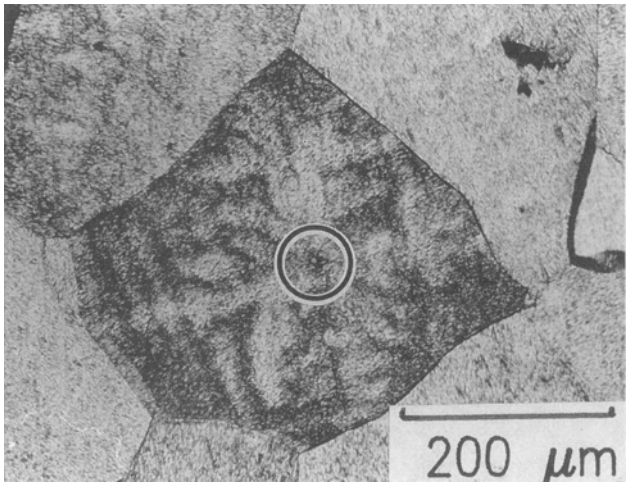


Fig. 8—Particle (circled) at the center of ferrite dendrite in welds containing 0.29 wt pct titanium and 0.040 pct aluminum.

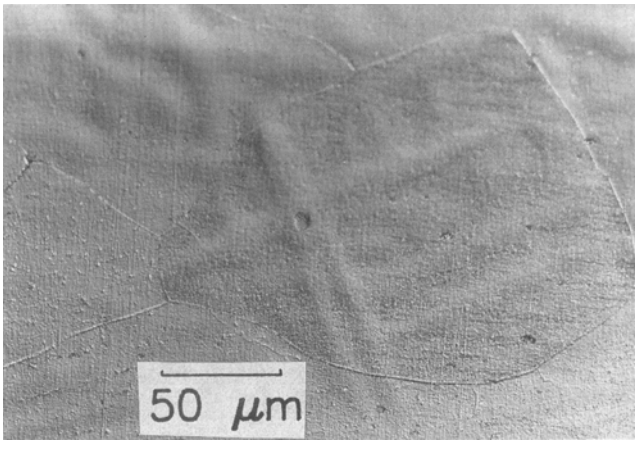


Fig. 9—Particle close to a dendrite center, as revealed by ion-beam etching and Nomarski microscopy.

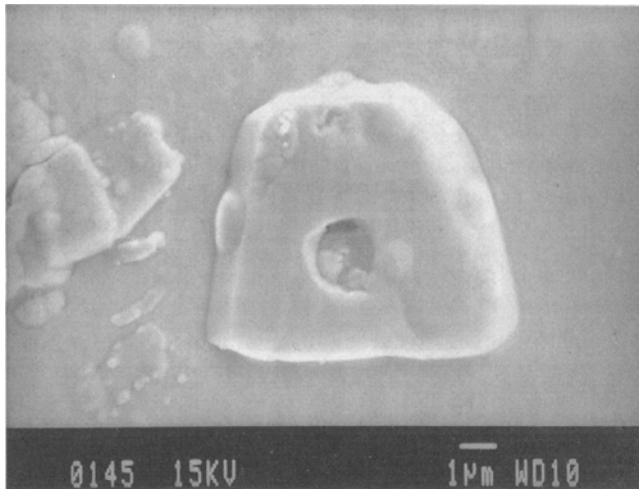


Fig. 10—Two-phase inclusion, with a central spherical region and outer more cuboidal phase.

**Table IV. Typical Measured Compositions of Inclusions (Atomic Percent)**

| Inclusion Type | Steel | Ti | Al | Ca | Mg | S |
|---|---|---|---|---|---|---|
| (a) Outer rims | 4091 | 100 | 0 | 0 | 0 | 0 |
| | 4092 | 91 | 0 | 1 | 0 | 0 |
| | | 75 | 0 | 25 | 0 | 0 |
| | 4093 | 100 | 0 | 0 | 0 | 0 |
| | | 60 | 0 | 28 | 0 | 2 |
| | 4094 | 100 | 0 | 0 | 0 | 0 |
| | | 46 | 0 | 0 | 54 | 0 |
| | 4095 | 100 | 0 | 0 | 0 | 0 |
| | | 90 | 0 | 0 | 10 | 0 |
| | | 40 | 0 | 0 | 60 | 0 |
| (b) Subparticles | 4092 | 28 | 0 | 15 | 57 | 0 |
| | | 55 | 0 | 5 | 40 | 0 |
| | 4093 | 78 | 0 | 13 | 0 | 9 |
| | | 55 | 0 | 33 | 0 | 12 |
| | 4094 | 11 | 48 | 41 | 0 | 0 |
| | 4095 | 69 | 31 | 0 | 0 | 0 |
| | | 38 | 6 | 0 | 56 | 0 |
| (c) Isolated | 4091 | 17 | 50 | 33 | 0 | 0 |
| | | 13 | 48 | 30 | 9 | 0 |
| | 4092 | 47 | 0 | 53 | 0 | 0 |
| | 4093 | 59 | 0 | 41 | 0 | 0 |

## V. DISCUSSION

### A. *The Effects of Composition*

The experimental evidence presented here clearly revealed that additions of minor elements such as titanium and aluminum play an important role in the occurrence of the CET during GTA welding of ferritic stainless steels. It was evident that increased Ti and Al levels increased the fraction of equiaxed grains and decreased the equiaxed grain size (Figures 2 through 5). Moreover, cuboidal Ti-rich particles were found at the center of equiaxed ferrite dendrites (Figure 8), providing direct support for heterogeneous nucleation as a factor in the CET.

From these observations, Ti-rich cuboidal particles can provide the nuclei responsible for the CET's of ferrite. The effect of the Ti level on the equiaxed grain size in the different steels (Figure 3) further supports this statement. The number of cuboids increased with increased levels of titanium (and aluminum) and qualitatively correlated with the decreases in equiaxed grain size.

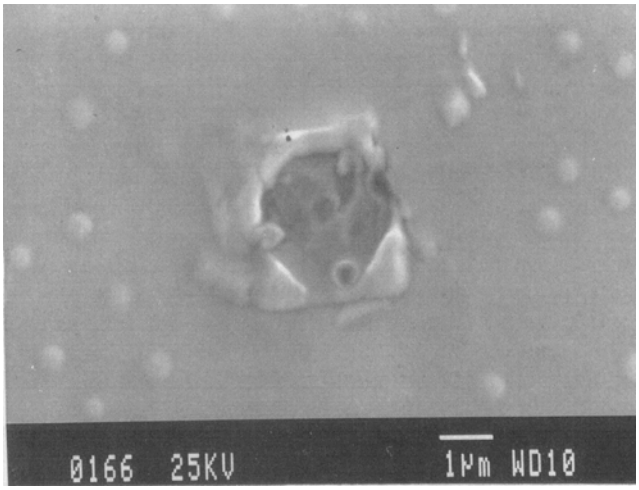


Fig. 11—Small "spherical" particle observed under high resolution conditions, showing outer rim.

**Table VI. Predicted Thermal Gradients at the Centerline**

| Welding Speed (mm/s) | Analytical (K/mm) | Numerical (K/mm) | Difference (Pct) |
|---|---|---|---|
| 3 | 23.9 | 7.6 | 68 |
| 8 | 20.6 | 6.2 | 70 |
| 14 | 15.8 | 4.0 | 74 |

**Table V. Welding Conditions and Parameters Used to Model Type 4091 Steel**

| Speed (mm/s) | Voltage (V) | Current (A) | $K_l$ Factor | $\eta$ (Pct) | $\sigma$ (mm) | Peak Temperature (K) |
|---|---|---|---|---|---|---|
| 3 | 10 | 143 | 2.5 | 73 | 2.3 | 2310 |
| 8 | 12 | 250 | 4.0 | 62 | 2.4 | 2420 |
| 14 | 13 | 360 | 5.0 | 60 | 2.6 | 2560 |

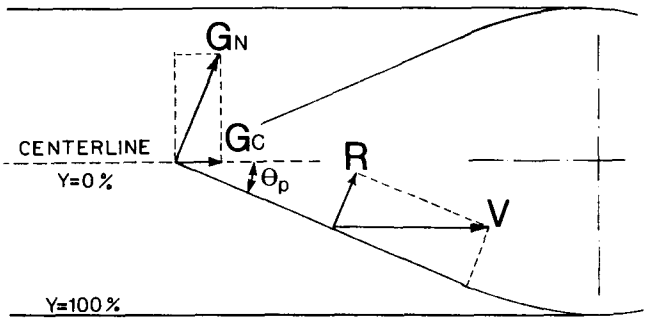


Fig. 12—Schematic diagram showing how the local values of $G$ and $R$ depend on $G_c$, welding speed, $V$, and the angle at the weld tail, $\theta_p$.

However, not all of the Ti-rich cuboidal particles observed were at the center of an equiaxed dendrite, which raises a question about the effectiveness of the nucleants. Heintze and McPherson[15] have also observed, in SA welds, that not all particles are effective nucleants. This may be related to the crystallographic faces presented to the melt, as well as to the local thermal conditions around the different particles.

The presence of aluminum, magnesium, calcium, and sulfur in spheroidal particles at the centers of cuboidal particles indicates that oxysulfides may, in turn, act as nucleants for the titanium-rich phase on which ferrite nucleates. The effect of aluminum, in particular, is supported by Figures 4 and 5. This is consistent with other work which showed Al-rich[15] or other phases[14] in Ti-rich phases. The present work indicates that other strong oxide or sulfide formers may be important in forming titanium-rich phases, even when the overall measured concentration of such residual elements is less than 30 ppm, as was the case for calcium in the present steels.

From extensive EDX analyses on the outer rim of many cuboidal particles, it is clear that their main component

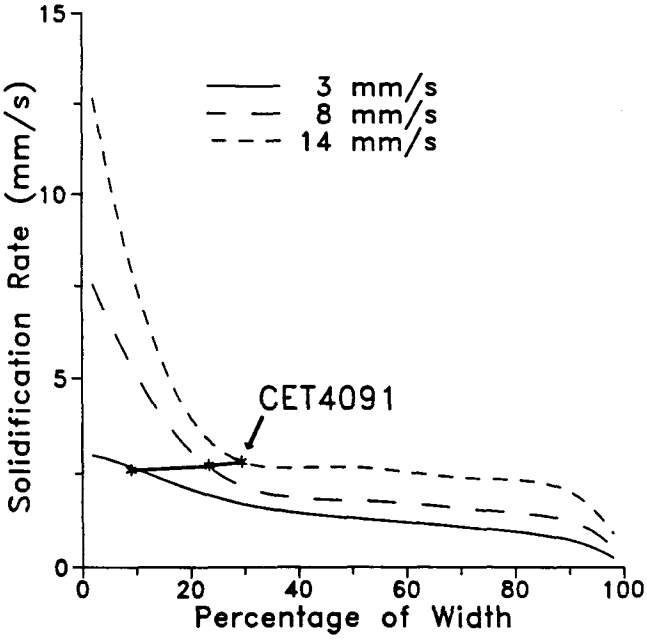


Fig. 13—Predicted values of $R$ as a function of distance from centerline for the different welding speeds.

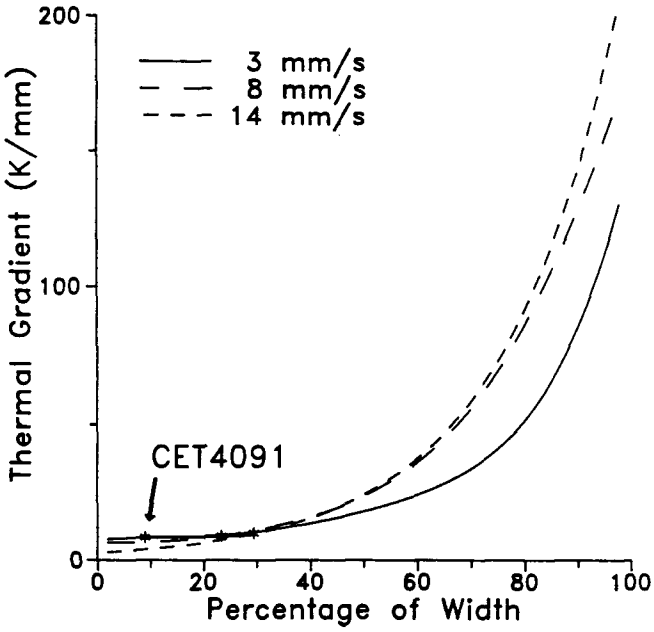


Fig. 14—Predicted values of $G$ as a function of distance from the centerline for the different welding speeds.

was titanium (at least for the elements which could be analyzed using the present equipment), and the observations of the yellow color of these cuboids identifies them as TiN or Ti(C, N) according to earlier authors.[14,15]

Many coarse cuboids were found only when both the nitrogen and titanium contents were high, supporting the deduction that they were TiN. Large cuboids also were found in the base metal, and it is believed that they were formed during the steelmaking process. Smaller cuboidal inclusions were favored by high titanium and aluminum contents and were more numerous in the weld metal than the base metal. It is believed that these smaller cuboidal particles form during cooling of the weld metal, nucleated on phases such as aluminum oxide.

Ostrowski and Langer[14] also suggested that sulfides formed on the outer rim of TiN particles may aid nucleation of ferrite, whereas Heintze and McPherson[15] did not find evidence to support this conclusion. High sulfur contents, as well as high Ca and Mg contents (strong sulfide formers), were found in the central subparticles of the relatively high S steel (4093) (Table IV). This alloy showed relatively little equiaxed grain formation. This, and the fact that sulfur was observed at the center of cuboidal particles, rather than at their rim, throws further doubt on the proposed role[14] of sulfide coatings on titanium-rich particles. However, the temperature at which sulfides form will depend on both the total sulfur content and the availability of strong sulfide formers. In the absence of such sulfide formers, more sulfur would remain in the liquid at lower temperatures and might then coat the cuboids. This aspect was not investigated in the present work.

In addition to the centers of cuboidal particles, particles with various percentages of Al, Ti, Ca, and Mg were detected as isolated spherical inclusions (Table IV). Due to their small size and chemistry, the image from spherical inclusions was extremely poor when the scanning

electron microscope was set up for analytical purposes. Under better image resolution conditions (not proper for analyses), many of the spherical particles appeared to have a tiny outer rim (Figure 11). This rim may be the source of titanium peaks in these small particles. Therefore, isolated "spherical" inclusions also may be surrounded by Ti-rich compounds which are in their early growth stage. This observation constitutes further strong evidence for the nucleation of the Ti-rich phase on Al-Ca-Mg-rich particles.

From this discussion, it becomes clear that details of the steelmaking process play a role in determining residual deoxidation products and, hence, the density of Ti-rich inclusions which aid grain refinement during welding. In particular, the aluminum and calcium contents, in addition to the titanium and nitrogen contents, may influence the subsequent weld structure.

### B. *Mechanisms of the Columnar-Equiaxed Transition*

The direct evidence of cuboidal particles at the center of dendrites supports the conclusion that heterogeneous nucleation can promote CET in GTA ferritic stainless steel welds. At low titanium contents, and especially low welding speeds, the equiaxed grains are limited to the surface regions (Table III).

In ingots, nucleation at free surfaces has been observed to contribute to equiaxed grains in aluminum alloys,[21,22] but in thin welded sheets, the grain structure has previously been found or assumed to be uniform through the thickness, with the exception of some equiaxed grains at the surfaces of magnetically stirred welds.[5,23] Nucleation near the surface may be favored in stainless steels compared to aluminum alloys, since the relatively high melting temperatures of the former would permit higher heat losses by radiation from the surface.

However, the high melting temperatures of the stainless steels are not sufficient to cause surface nucleation, since without titanium additions, the welds were entirely columnar at the low welding speed (Figure 1). At increased welding speeds, even the low titanium alloys showed some equiaxed surface grains (Table III and Figure 7), but the equiaxed grain size decreased with titanium content (Figure 3), again supporting the proposed mechanism of heterogeneous nucleation by Ti-rich particles.

Since other workers have proposed that equiaxed grains occur by dendrite fragmentation, careful metallographic examination of the centers of such grains was carried out, using both ion-beam etching and repetitive polishing and chemical etching. No direct evidence was found for such fragmentation. In a given section, many equiaxed grains did not reveal central particles, but this is not surprising, considering the small size of the particles and the difficulties in keeping the particles in place during etching, as discussed earlier. On the contrary, the direct evidence of central particles in some equiaxed grains is taken as strong support for heterogeneous nucleation.

At sufficiently high titanium levels, approximately constant fractions of equiaxed grains were found through the thickness of the welds for all welding speeds (Table III). This suggests that in these alloys, the formation of equiaxed grains is a bulk effect; *i.e.*, that the grains are grown in place, rather than originating only near the top surface.

### C. *The Effects of Welding Conditions*

From the thermal point of view, the fraction of equiaxed grains was observed to be controlled by the welding speed. Increasing the welding speed promoted the CET in alloys containing Ti-rich nucleating particles. Similar observations have been reported for aluminum GTA welds.[2,6,7,8]

The presence of heterogeneous nuclei ahead of the columnar array does not guarantee the CET. Some critical thermal conditions must be also fulfilled, which are favored by increased welding speeds (Figures 2, 4, and 6). The welding conditions affect the local solidification parameters, namely, the liquid thermal gradient, $G$, and the solidification velocity, $R$, normal to the growing interface, by affecting the heat transfer conditions in the weld pool. Qualitatively, it has been recognized for some time that there is a gradual increase in $R$ and a decrease in $G$ as solidification proceeds from the fusion boundary to the centerline of a weld.[1,6,8,17]

Analytical solutions of the temperature profiles were used by Kato *et al.*[17] in trying to analyze the effects of the welding parameters on $G$ and $R$ in aluminum welds to explain the CET at high welding speeds. However, since this approach did not include latent heat effects, the actual values must always be in error, despite the complexity of calculations. Unfortunately, the error in ignoring the latent heat on the positions of the isotherms is greatest near the weld tail at high speeds, the very position and conditions which promote the CET.

An approximate analytical expression for the thermal gradient along the centerline, $G_c$, has been used previously in estimating $G$ along the solid-liquid interface.[6,8] Experimentally, this has been found to be in some error, because of the inherent assumptions in deriving the expression,[8] but especially at low welding speeds, it provides a simple tool to predict the trends, as will be examined below. However, since the CET does not occur right at the centerline, but some distance from it, there are obvious limitations in using $G_c$ and $R$ at the centerline as a criterion for the initiation of the CET, especially when the weld pool becomes teardrop-shaped. This stresses the limitations of the approach used by Kou and Le[8] for Al welds in trying to predict a critical $G/R$ ratio for the initiation of the CET in weld pool solidification. They used an average $G$ measured along the centerline and assumed $R$ equal to the welding speed. For a teardrop-shaped weld pool, the local values of $G$ and $R$ close to the centerline could be better estimated if the angle, $\theta_p$, between the pool boundary at the tail and the centerline axis is known, as illustrated in Figure 15. This, of course, leads to higher calculated values of thermal gradient and to lower values of solidification velocity. The following relationships were previously suggested by Ganaha *et al.*:[6]

$$G = \frac{G_c}{\sin \theta_p} \qquad [2]$$

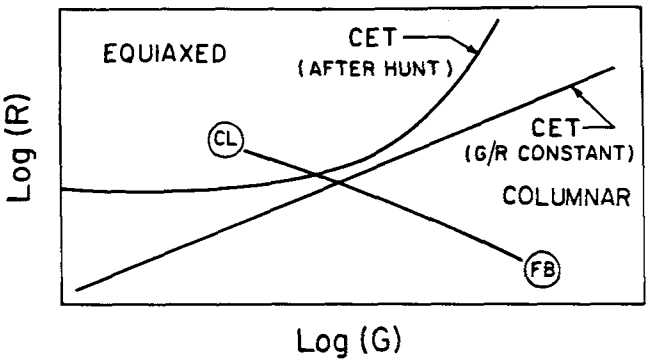


Fig. 15—Schematic of the variation of the weld thermal conditions from the fusion boundary (FB) to the centerline (CL) plotted as log $R$ *vs* log $G$. Lines for the CET according to constant $G/R$ and Hunt's model[24] are also shown.

and

$$R = v \sin \theta_p \qquad [3]$$

However, the values of $G$ calculated using Eq. [2] will be in considerable error when the CET occurs more than a small fraction of the weld width from the centerline. Moreover, the values of $\theta_p$ are not known *a priori*, and the effect of latent heat is not included in the estimates of $G_c$.

In this work, the finite element heat transfer model briefly described above and more fully elsewhere[18] was used to estimate values of $G$ and $R$ along the weld solidification front after matching the model to the observed length and widths of the welds. The thermal gradient at the tail of the weld pool from the finite element analysis is compared with that predicted by Eq. [1] in Table VI. The liquid thermal gradients predicted by the finite element model (FEM) at the interface are significantly lower than those from the analytical solution, and the difference increases with welding speed. This is probably due to the evolution of the latent heat of fusion which is included in the FEM. Considering the factors ignored in calculating $G_c$, it is seen to be a reasonable estimate at sufficiently low speeds and certainly much simpler than the numerical FEM estimate. However, as discussed above, it does not give the value of $G$ where the CET takes place.

The effects of the welding conditions on the distribution of $R$ and $G$ along the weld pool edge for type 409 steel, as predicted by the finite element approach, are shown in Figures 13 and 14, respectively, in which the horizontal axis is the distance from the centerline (in percentage), as defined in Figure 12. The equiaxed fraction measured for the type 4091 steel for each welding speed has been marked with an asterisk defining a line labeled "CET4091" in these figures. Figure 13 shows that the solidification rate at the edge of the equiaxed region increases only slightly with increasing welding speed, from about 2.6 to 2.95 mm/s. In fact, the CET line intersects the plots of the two higher welding speeds at the beginning of the plateau discussed earlier. Similarly, in Figure 14, the thermal gradient at the edge of the equiaxed region is seen to increase with welding speed from about 8.5 K to 9.8 K/mm. This is also a small variation, of the order of the uncertainty in the numerical results. There is nevertheless a clear qualitative trend suggesting how the welding conditions influence the CET. Figures 13 and 14 indicate that for fixed welding conditions, the equiaxed grains grow (if at all) in the region of lower $G$ and higher $R$ which is close to the centerline. The extent of this "favorable" region increases with welding speed, hence increasing the equiaxed fraction.

The combination of these numerical and experimental results allows some comparisons with existing models for the CET. The theory of constitutional supercooling is useful in explaining the instability of a *planar* solid-liquid interface but does not explain the origin of equiaxed grains *vs* columnar grains. Nevertheless, in most cases, the CET during welding has been explained using constitutional supercooling theory alone.

It is clear that the CET in welds occurs close to the centerline, where the solidification rate $R$ increases and the thermal gradient $G$ decreases; *i.e.*, $G/R$ decreases. If a minimum $G/R$ criterion is sufficient to explain the CET, then the transition should occur as a straight line in a plot of log $G$ *vs* log $R$, as illustrated in Figure 15.

More recently, however, Hunt[24] has proposed a more comprehensive analytical model to account for the CET in controlled solidification of Al-Cu alloys. He assumed that the CET occurs when the volume fraction of growing equiaxed grains ahead of the columnar array reaches a critical value. This, in turn, is possible when sufficient columnar growth undercooling, $\Delta T_c$, and a sufficient number of heterogeneous nucleating sites, $N_0$, are both provided. For a given alloy, $N_0$ is fixed, but sufficient growth undercooling for their growth to block columnar grains will only be possible above a critical columnar solidification velocity. The time available for their growth depends on the temperature gradient, giving an equiaxed region on a plot of log $G$ *vs* log $R$ of the shape shown in Figure 15, according to Hunt's calculations.

In welds, the thermal conditions change from high $G$-low $R$ conditions at the fusion boundary to low $G$-higher $R$ values approaching the centerline, as illustrated in Figure 15. The intersection of the line plotting the local solidification conditions in the weld with the transition line for the CET will indicate where the CET will take place. Essentially, according to the above model by Hunt,[24] the critical $G$ and $R$ conditions required for the CET depend on the extent of columnar growth undercooling and the number and efficiency of heterogeneous nuclei ahead of the columnar array.

The observations made during the course of the present work are consistent with several aspects of this model. First, the position of the CET on the log $G$-log $R$ plot depend on the number of nuclei, $N_0$. Increased values of $N_0$ shift the transition to higher values of $G$.[24] For a given welding condition, this means that the CET transition line and the line plotting the thermal conditions from the fusion boundary to the centerline will intersect closer to the fusion boundary, hence increasing the equiaxed fraction. The observed effects of titanium and aluminum on the fraction and size of equiaxed grain indicate that these alloy additions increase $N_0$. At low additions of these elements, $N_0$ is so low that either the CET does not occur at all, or it occurs only close to the free surface where it is favored by radiation losses.

Second, at high values of Ti and Al additions, the CET

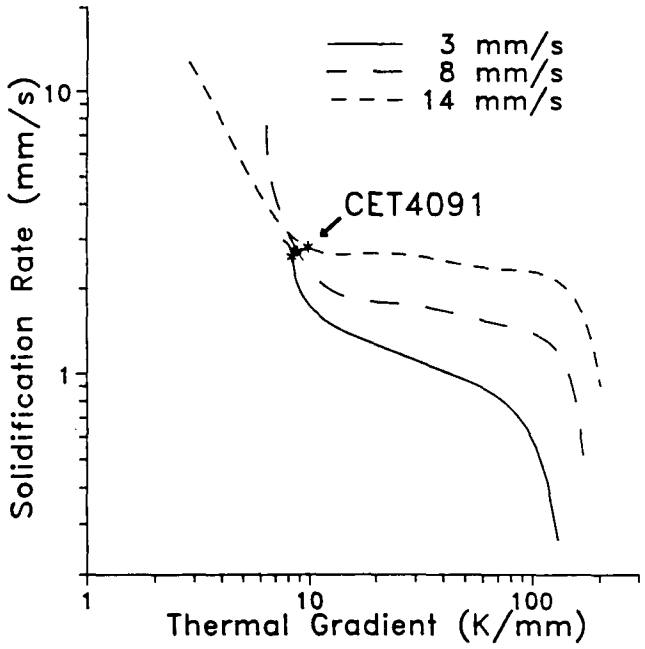


Fig. 16—Plot of predicted log $R$ *vs* log $G$ for the different welding speeds.

occurs near the centerline due to the low values of $G$ and high values of $R$ in that region. Increased welding speed shifted the predicted thermal conditions near the centerline toward higher $R$ and lower $G$, according to the thermal model (Figures 13 and 14). This increases the equiaxed fraction, consistent with the model. The predicted $G$ *vs* $R$ values for the three welding conditions are shown in Figure 16 using logarithmic scales. The line for the CET in steel 4091 is also shown in this figure. Its points of intersection with the three plots lie very close in the figure, since the thermal conditions at the CET are similar for the three welding conditions, as shown in Figures 13 and 14. However, since the constitutional supercooling model does not discuss the origins of the equiaxed grains, it does not explain the observed compositional effects of Ti and Al.

## VI. CONCLUSIONS

The CET in GTA welds completely penetrating sheets of ferritic stainless steels was favored by increases in titanium and aluminum, as well as by increases in welding speeds (for an approximately constant weld width).

In steels containing less than 0.29 wt pct Ti and 0.040 wt pct Al, increased welding speed promoted equiaxed grains near the weld surfaces, but columnar grains remained at the centerline in the interior of the sheet.

Cuboidal Ti-rich particles, probably TiN, have been observed at the centers of equiaxed dendrites and are believed to be the nucleating phase for such dendrites. However, not all such particles act as nucleants.

Within the Ti-rich particles, other spherical phases are present which may be rich in Al, Ca, Mg, and S, depending on the steel's composition. These are believed to be oxides and/or sulfides which act as nucleants for the Ti-rich phase.

The results of a numerical analysis of the thermal conditions, including latent heat effects, were used to predict the local temperature gradient, $G$, and solidification velocity, $R$, along the weld edge for different weld conditions.

The effects of composition (*i.e.*, increased numbers of nucleants) and welding speed are consistant with a model by Hunt,[24] which predicts the CET when sufficient nuclei are present and the temperature gradient falls below a critical value which depends on $R$.

## ACKNOWLEDGMENTS

J.C. Villafuerte was supported by a fellowship from the International Development Research Centre of Canada during this work. This work forms part of a research agreement between the University of Waterloo and the Universidad del Valle in Cali, Colombia, supported by IDRC. E. Pardo had a scholarship from CONICET in Argentina. Support was also provided by the Natural Sciences and Engineering Research Council of Canada. Materials were provided by Associated Tube Industries Inc., Markham, Ontario, and Atlas Steels, Tracy, Quebec, who also provided chemical analysis of the steels. Technical support by P. Caple, H. Kamler, and N. Wilhelm is also gratefully acknowledged.

## REFERENCES

1. G.J. Davies and J.G. Garland: *Int. Metall. Rev.*, 1975, vol. 20, pp. 83-106.
2. F. Matsuda, H. Nakagawa, K. Nakata, and R. Ayani: *Trans. JWRI*, 1978, vol. 7, pp. 111-27.
3. F. Matsuda, K. Nakata, and N. Sano: *Trans. JWRI*, 1986, vol. 15, pp. 155-66.
4. M.A. Abralov and R.U. Abdurakhmanov: *Autom. Weld.*, 1982, no. 2, pp. 18-21.
5. B.P. Pearce and H.W. Kerr: *Metall. Trans. B*, 1981, vol. 12B, pp. 479-89.
6. T. Ganaha, B.P. Pearce, and H.W. Kerr: *Metall. Trans. A*, 1980, vol. 11A, pp. 1351-59.
7. S. Kou and Y. Le: *Weld. J.*, 1986, vol. 65, pp. 305s-313s.
8. S. Kou and Y. Le: *Metall. Trans. A*, 1988, vol. 19A, pp. 1075-82.
9. F. Matsuda, K. Nakata, Y. Miyanaga, T. Kayano, and K. Tsukamoto: *Trans. JWRI*, 1978, vol. 7, pp. 33-44.
10. Bruce L. Bramfitt: *Metall. Trans.*, 1970, vol. 1, pp. 1987-95.
11. G.K. Turnbull, P.M. Patton, G.W. Form, and J.F. Wallace: *Trans. Am. Foundrymen's Soc.*, 1961, vol. 69, pp. 792-804.
12. J.G. Garland: *Met. Constr.*, 1974, vol. 6, pp. 121-27.
13. D.C. Willingham and N. Bailey: *Weld. Res. Int.*, 1977, vol. 7, pp. 28-45.
14. A. Ostrowski and E.W. Langer: *Scand. J. Metall.*, 1979, vol. 8, pp. 153-60.
15. G.N. Heintze and R. McPherson: *Weld. J.*, 1986, vol. 65, pp. 71s-82s.
16. J.M. McTighe and J. Beech: *Metallography*, 1977, vol. 10, pp. 363-70.
17. M. Kato, F. Matsuda, and T. Senda: *Trans. Jpn. Weld. Soc.*, 1972, vol. 3, pp. 69-76.
18. E. Pardo and D.C. Weckman: in *Modeling and Control of Casting and Welding Processes IV*, A.F. Giamei and G.J. Abbaschian, eds., TMS, Warrendale, PA, 1988, pp. 187-95.
19. H.J. Kraus: *J. Heat Transfer*, 1986, vol. 108, pp. 591-96.
20. N.S. Tsai and T.W. Eagar: *Metall. Trans. B*, 1985, vol. 16, pp. 841-46.
21. G.S. Cole and G.F. Bolling: *Trans. TMS-AIME*, 1969, vol. 245, pp. 725-34.
22. R.T. Southin: *Trans. TMS-AIME*, 1967, vol. 239, pp. 220-25.
23. T. Ganaha and H.W. Kerr: *Metall. Trans. B*, 1978, vol. 9B, pp. 313-16.
24. J.D. Hunt: *Mater. Sci. Eng.*, 1984, vol. 65, pp. 75-83.